Hadronic Cross sections: from cyclotrons to colliders to cosmic rays

M. M. Block
Department of Physics and Astronomy,
Northwestern University, Evanston, IL 60208,

Paper presented at the 2010 ISVHECRI conference,
FermiLab, June 28—July 2, 2020

(Dated: September 1, 2010)

We present evidence for the saturation of the Froissart bound at high energy for *all hadronic* total cross sections at high energies, and use this to unify pp (and $\bar{p}p$) total cross sections over the energy range from cyclotrons to colliders to ultra-high energy cosmic rays, an energy span from $\sqrt{s} = 4$ GeV to 80 TeV.

Introduction. High energy cross sections for the scattering of hadrons should be bounded by $\sigma \sim \ln^2 s$, where s is the square of the cms energy. This fundamental result is derived from unitarity and analyticity by Froissart [1], who states:

"At forward or backward angles, the modulus of the amplitude behaves at most like $s \ln^2 s$, as s goes to infinity. We can use the optical theorem to derive that the total cross sections behave at most like $\ln^2 s$, as s goes to infinity".

In this context, saturating the Froissart bound refers to an energy dependence of the total cross section rising no more rapidly than $\ln^2 s$.

It will be shown that the Froissart bound is *saturated* at high energies in γp, $\pi^{\pm} p$ and $\bar{p}p$ and pp scattering [2], as well as in $\gamma^* p$ scattering [3], as seen from Deep Inelastic Scattering (DIS) in $e + p \to e + X$.

Using Finite Energy Sum Rules (FESR) derived from analyticity constraints—in order to anchor accurately cross sections at cyclotron energies [4]—we will make precise predictions about the total pp cross section, the ρ-value (the ratio of the real to the imaginary portion of the forward pp scattering amplitude), as well as the shape of the differential elastic scattering cross section, $d\sigma_{rmeel}/dt$, at the LHC. Further, we will make predictions of the total pp cross section at cosmic ray energies, up to 50 TeV, and will compare them to the latest experiments.

Data selection. We make the following major assumptions about the experimental data that we fit:

1. The experimental data can be fitted by a model which successfully describes the data.

2. The signal data are Gaussianly distributed, with Gaussian errors.

3. The noise data consists only of points "far away" from the true signal, *i.e.*, "outliers" only.

4. The outliers do not completely swamp the signal data.

We will use the "Sieve" algorithm [5] to remove "outliers" in the cross section and ρ-values that we will fit, in order to improve the accuracy of our fits. The "Sieve" Algorithm does the following:

1. Make a robust fit of *all* of the data (presumed outliers and all) by minimizing Λ_0^2, the Lorentzian squared, defined as

$$\Lambda_0^2(\boldsymbol{\alpha}; \boldsymbol{x}) \equiv \sum_{i=1}^{N} \ln\left\{1 + 0.179 \Delta\chi_i^2(x_i; \boldsymbol{\alpha})\right\},$$
$$\text{where } \Delta\chi_i^2(x_i; \boldsymbol{\alpha}) \equiv \left(\frac{y_i - y(x_i; \boldsymbol{\alpha})}{\sigma_i}\right)^2. \qquad (1)$$

   The M-dimensional parameter space of the fit is given by $\boldsymbol{\alpha} = \{\alpha_1, \ldots, \alpha_M\}$; $\boldsymbol{x} = \{x_1, \ldots, x_N\}$ is the abscissa of the N experimental measurements $\boldsymbol{y} = \{y_1, \ldots, y_N\}$ that are being fit; $y(x_i; \boldsymbol{\alpha})$ is the theoretical value at x_i and σ_i is the experimental error. Minimizing Λ_0^2 gives the same total $\chi^2_{\rm min} \equiv \sum_{i=1}^{N} \Delta\chi_i^2(x_i; \boldsymbol{\alpha})$ as that found in a χ^2 fit, as well as rms widths (errors) for the parameters—*for Gaussianly distributed data*—that are almost the same as those found in a χ^2 fit. The quantitative measure of "far away" from the true signal, *i.e.,* point i is an outlier, is the magnitude of its $\Delta\chi_i^2(x_i; \boldsymbol{\alpha}) = \left(\frac{y_i - y(x_i; \boldsymbol{\alpha})}{\sigma_i}\right)^2$.

   If $\chi^2_{\rm min}$ is satisfactory, make a conventional χ^2 fit to get the errors and you are finished. If $\chi^2_{\rm min}$ is not satisfactory, proceed to step 2.

2. Using the above robust Λ_0^2 fit as the initial estimator for the theoretical curve, evaluate $\Delta\chi_i^2(x_i; \boldsymbol{\alpha})$, for each of the N experimental points.

3. A largest cut, $\Delta\chi_i^2(x_i; \boldsymbol{\alpha})_{\rm max}$, must now be selected. For example, we might start the process with $\Delta\chi_i^2(x_i; \boldsymbol{\alpha})_{\rm max} = 9$. If any of the points have $\Delta\chi_i^2(x_i; \boldsymbol{\alpha}) > \Delta\chi_i^2(x_i; \boldsymbol{\alpha})_{\rm max}$, reject them—they fell through the "Sieve". The choice of $\Delta\chi_i^2(x_i; \boldsymbol{\alpha})_{\rm max}$ is an attempt to pick the largest

"Sieve" size (largest $\Delta\chi_i^2(x_i;\boldsymbol{\alpha})_{\rm max}$) that rejects all of the outliers, while minimizing the number of signal points rejected.

4. Next, make a conventional χ^2 fit to the sifted set—these data points are the ones that have been retained in the "Sieve". This fit is used to estimate $\chi^2_{\rm min}$. Since the data set has been truncated by eliminating the points with $\Delta\chi_i^2(x_i;\boldsymbol{\alpha}) > \Delta\chi_i^2(x_i;\boldsymbol{\alpha})_{\rm max}$, we must slightly renormalize the $\chi^2_{\rm min}$ found to account for this, by the factor $\mathcal{R}$=1.027, 1.14, 1.291 for $\Delta\chi^2_{i\,\rm max} = 9, 6, 4$. If the renormalized $\chi^2_{\rm min}$, *i.e.,* $\mathcal{R}\times\chi^2_{\rm min}$ is acceptable—in the *conventional* sense, using the χ^2 distribution probability function—we consider the fit of the data to the model to be satisfactory and proceed to the next step. If the renormalized $\chi^2_{\rm min}$ is not acceptable and $\Delta\chi_i^2(x_i;\boldsymbol{\alpha})_{\rm max}$ is not too small, we pick a smaller $\Delta\chi_i^2(x_i;\boldsymbol{\alpha})_{\rm max}$ and go back to step 3. The smallest value of $\Delta\chi_i^2(x_i;\boldsymbol{\alpha})_{\rm max}$ that makes much sense, in our opinion, is $\Delta\chi_i^2(x_i;\boldsymbol{\alpha})_{\rm max} > 2$. One of our primary assumptions is that the noise doesn't swamp the signal. If it does, then we must discard the model—we can do nothing further with this model and data set!

5. From the χ^2 fit that was made to the "sifted" data in the preceding step, evaluate the parameters $\boldsymbol{\alpha}$. Next, evaluate the $M\times M$ covariance (squared error) matrix of the parameter space found in the χ^2 fit. We find the *renormalized* squared error matrix of our χ^2 fit by multiplying the covariance matrix by the square of the factor r_{χ^2} (we find $r_{\chi^2}\sim 1.02, 1.05$, 1.11 and 1.14 for $\Delta\chi_i^2(x_i;\boldsymbol{\alpha})_{\rm max} = 9$, 6, 4 and 2). The values of $r_{\chi^2} > 1$ reflect the fact that a χ^2 fit to the *truncated* Gaussian distribution that we obtain has a rms (root mean square) width which is somewhat greater than the rms width of the χ^2 fit to the same untruncated distribution. Extensive computer simulations demonstrate that this *robust* method of error estimation yields accurate error estimates and error correlations, even in the presence of large backgrounds.

You are now finished. The initial robust Λ_0^2 fit has been used to allow the phenomenologist to find a sifted data set. The subsequent application of a χ^2 fit to the *sifted set* gives stable estimates of the model parameters $\boldsymbol{\alpha}$, as well as a goodness-of-fit of the data to the model when $\chi^2_{\rm min}$ is renormalized for the effect of truncation due to the cut $\Delta\chi_i^2(x_i;\boldsymbol{\alpha})_{\rm max}$. Model parameter errors are found when the covariance (squared error) matrix of the χ^2 fit is multiplied by the appropriate factor $(r_{\chi^2})^2$ for the cut $\Delta\chi_i^2(x_i;\boldsymbol{\alpha})_{\rm max}$.

Analyticity constraints on hadronic cross sections. Block and Cahn [7] used an even real analytic amplitude $\tilde{f}_+(\nu)$ given by

$$\begin{aligned}
{\rm Im}\,\tilde{f}_+(\nu) &= \frac{p}{4\pi}\left[c_0 + c_1\ln\left(\frac{\nu}{m}\right) + c_2\ln^2\left(\frac{\nu}{m}\right) \right.\\
&\quad \left. + \beta_{\mathcal{P}'}\left(\frac{\nu}{m}\right)^{\mu-1}\right] \quad \text{for } \nu \geq m,\\
{\rm Im}\,\tilde{f}_+(\nu) &= 0 \qquad \text{for } 0 \leq \nu \leq m, \qquad (2)\\
{\rm Re}\,\tilde{f}_+(\nu) &= \frac{p}{4\pi}\left[\frac{\pi}{2}c_1 + c_2\pi\ln\left(\frac{\nu}{m}\right)\right.\\
&\quad \left. - \beta_{\mathcal{P}'}\cot\left(\frac{\pi\mu}{2}\right)\left(\frac{\nu}{m}\right)^{\mu-1}\right], \qquad (3)
\end{aligned}$$

where ν is the nucleon (pion) laboratory energy and m is the proton mass. Using the optical theorem, the even cross section is

$$\tilde{\sigma}_+(\nu) = c_0 + c_1\ln(\nu/m) + c_2\ln^2(\nu/m) + \beta_{\mathcal{P}'}(\nu/m)^{\mu-1}, \qquad (4)$$

where here the coefficients c_0, c_1, c_2 and $\beta_{\mathcal{P}'}$ have dimensions of mb. Since $\frac{\nu}{m} = \frac{s}{2m^2}$ for $\nu \gg m$, i.e., for the high energy regime in which we are working, we will henceforth refer to equations similar to that of Eq. (4) as $\ln^2 s$ fits if $c_2 \neq 0$ and as $\ln s$ fits if $c_2 = 0$.

We now introduce $f_+(\nu)$, the *true* even forward scattering amplitude (which of course, we do not know!), valid for all ν, where $f_+(\nu) \equiv [f_{pp}(\nu) + f_{\bar{p}p}(\nu)]/2$, using forward scattering amplitudes for pp and $\bar{p}p$ collisions. Using the optical theorem, the imaginary portion of $f_+(\nu)$ is related to the even total cross section $\sigma_{\rm even}(\nu)$ by

$${\rm Im}\,f_+(\nu) = \frac{p}{4\pi}\sigma_{\rm even}(\nu) \qquad \text{for } \nu \geq m. \qquad (5)$$

Next, define the odd amplitude $\nu\hat{f}_+(\nu)$ as the difference

$$\nu\hat{f}_+(\nu) \equiv \nu\left[f_+(\nu) - \tilde{f}_+(\nu)\right], \qquad (6)$$

which satisfies the unsubtracted odd amplitude dispersion relation

$${\rm Re}\,\nu\hat{f}_+(\nu) = \frac{2\nu}{\pi}\int_0^\infty \frac{{\rm Im}\,\nu'\hat{f}_+(\nu')}{\nu'^2 - \nu^2}\,d\nu'. \qquad (7)$$

Since for large ν, the odd amplitude $\nu\hat{f}_+(\nu) \sim \nu^\alpha$ ($\alpha < 0$) by design, it also satisfies the super-convergence relation

$$\int_0^\infty {\rm Im}\,\nu\hat{f}_+(\nu)\,d\nu = 0. \qquad (8)$$

In Ref. [8], the FESRs are given by

$$\int_0^{\nu_0}\nu^n\,{\rm Im}\hat{f}\,d\nu = \sum\frac{{\nu_0}^{\alpha+n+1}}{\alpha+n+1}, \quad n = 0, 1, \ldots, \infty, \qquad (9)$$

where $\hat{f}(\nu)$ is crossing-even for odd integer n and crossing-odd for even integer n. In analogy to the $n = 1$ FESR of Ref.. [8], which requires the odd amplitude

$\nu\hat{f}(\nu)$, Igi and Ishida inserted the super-convergent amplitude of Eq. (6) into the super-convergent dispersion relation of Eq. (8), obtaining

$$\int_0^\infty \nu \,\mathrm{Im}\,\left[f_+(\nu) - \tilde{f}_+(\nu)\right] d\nu. \tag{10}$$

We note that the odd difference amplitude $\nu \mathrm{Im}\,\hat{f}_+(\nu)$ satisfies Eq. (8), a super-convergent dispersion relation, even if neither $\nu\,\mathrm{Im}\,f_+(\nu)$ nor $\nu\,\mathrm{Im}\,\tilde{f}_+(\nu)$ satisfies it. Since the integrand of Eq. (10), $\nu\,\mathrm{Im}\,\left[f_+(\nu) - \tilde{f}_+(\nu)\right]$, is super-convergent, we can truncate the upper limit of the integration at the finite energy ν_0, an energy high enough for resonance behavior to vanish and where the difference between the two amplitudes—the true amplitude $f_+(\nu)$ minus $\tilde{f}_+(\nu)$, the amplitude which parametrizes the high energy behavior—becomes negligible, so that the integrand can be neglected for energies greater than ν_0. Thus, after some rearrangement, we get the even finite energy sum rule (FESR)

$$\int_0^{\nu_0} \nu \mathrm{Im}\, f_+(\nu)\, d\nu = \int_0^{\nu_0} \nu \mathrm{Im}\, \tilde{f}_+(\nu)\, d\nu. \tag{11}$$

Next, the left-hand integral of Eq. (11) is broken up into two parts, an integral from 0 to m (the 'unphysical' region) and the integral from m to ν_0, the physical region. We use the optical theorem to evaluate the left-hand integrand for $\nu \geq m$. After noting that the imaginary portion of $\tilde{f}_+(\nu) = 0$ for $0 \leq \nu \leq m$, we again use the optical theorem to evaluate the right-hand integrand, finally obtaining the finite energy sum rule FESR(2) of Igi and Ishida [6], in the form:

$$\int_0^m \nu\,\mathrm{Im}\,f_+(\nu)\,d\nu + \frac{1}{4\pi}\int_m^{\nu_0} \nu p\,\sigma_{\mathrm{even}}(\nu)\,d\nu = \frac{1}{4\pi}\int_m^{\nu_0} \nu p\,\tilde{\sigma}_+(\nu)\,d\nu. \tag{12}$$

We now enlarge on the consequences of Eq. (12). We note that if Eq. (12) is valid at the upper limit ν_0, it certainly is also valid at $\nu_0 + \Delta\nu_0$, where $\Delta\nu_0$ is very small compared to ν_0, i.e., $0 \leq \Delta\nu_0 \ll \nu_0$. Evaluating Eq. (12) at the energy $\nu_0 + \Delta\nu_0$ and then subtracting Eq. (12) evaluated at ν_0, we find

$$\frac{1}{4\pi}\int_{\nu_0}^{\nu_0+\Delta\nu_0} \nu p\,\sigma_{\mathrm{even}}(\nu)\,d\nu = \frac{1}{4\pi}\int_{\nu_0}^{\nu_0+\Delta\nu_0} \nu p\tilde{\sigma}_+(\nu)\,d\nu. \tag{13}$$

Clearly, in the limit of $\Delta\nu_0 \to 0$, Eq. (13) goes into

$$\sigma_{\mathrm{even}}(\nu_0) = \tilde{\sigma}_+(\nu_0). \tag{14}$$

Obviously, Eq. (14) also implies that

$$\sigma_{\mathrm{even}}(\nu) = \tilde{\sigma}_+(\nu) \qquad \text{for all } \nu \geq \nu_0, \tag{15}$$

but is most useful in practice when ν_0 is as low as possible. The utility of Eq. (15) becomes evident when we recognize that the left-hand side of it can be evaluated using the very accurate low energy *experimental* crossing-even total cross section data, whereas the right-hand side can use the phenomenologist's parameterization of the *high* energy cross section. For example, we could use the cross section parameterization of Eq. (4) on the right-hand side of Eq. (15) and write the constraint

$$[\sigma_{pp}(\nu) + \sigma_{\bar{p}p}(\nu)]/2 = c_0 + c_1 \ln(\nu/m) + c_2 \ln^2(\nu/m) + \beta_{\mathcal{P}'}(\nu/m)^{\mu-1}, \tag{16}$$

where σ_{pp} and $\sigma_{\bar{p}p}(\nu)$ are the *experimental pp* and $\bar{p}p$ cross sections at the laboratory energy ν. Equation (14) (or Eq. (15)) is our first important extension, giving us an analyticity constraint, a consistency condition that the even high energy (asymptotic) amplitude must satisfy.

Reiterating, Eq. (15) is a consistency condition imposed by analyticity that states that we must fix the even high energy cross section evaluated at energy $\nu \geq \nu_0$ (using the asymptotic even amplitude) to the low energy experimental even cross section at the *same* energy ν, where ν_0 is an energy just above the resonances. Clearly, Eq. (14) also implies that all derivatives of the total cross sections match, as well as the cross sections themselves, i.e.,

$$\frac{d^n\sigma_{\mathrm{even}}}{d\nu^n}(\nu) \;=\; \frac{d^n\tilde{\sigma}_+}{d\nu^n}(\nu),\; n = 0, 1, 2, \ldots\; \nu \geq \nu_0, \tag{17}$$

giving new even amplitude analyticity constraints. Of course, the evaluation of Eq. (17) for $n = 0$ and $n = 1$ is effectively the same as evaluating Eq. (17) for $n = 0$ at two nearby values, ν_0 and $\nu_1 > \nu_0$. It is up to the phenomenologist to decide which *experimental set* of quantities it is easier to evaluate.

We emphasize that these consistency constraints are the consequences of imposing analyticity, implying several important conditions:

1. The new constraints that are derived here tie together both the even hh and $\bar{\mathrm{h}}$h experimental cross sections and their derivatives to the even high energy approximation that is used to fit data at energies well above the resonance region. Analyticity then requires that there should be a *good* fit to the high energy data *after* using these constraints, i.e., the χ^2 per degree of freedom of the constrained fit should be ~ 1, *if* the high energy asymptotic amplitude is a good approximation to the high energy data. This is our consistency condition demanded by analyticity. If, on the other hand, the high energy asymptotic amplitude would have given a somewhat poorer fit to the data when *not* using the new constraints, the effect is tremendously magnified by utilizing these new constraints, yielding a

very large χ^2 per degree of freedom. As an example, both Block and Halzen [2] and Igi and Ishida [6] *conclusively* rule out a $\ln s$ fit to both $\pi^{\pm}p$ and pp and $\bar{p}p$ cross sections and ρ-values because it has a huge χ^2 per degree of freedom.

2. Consistency with analyticity requires that the results be valid for all $\nu \geq \nu_0$, so that the constraint doesn't depend on the particular choice of ν.

3. The non-physical integral $\int_0^m \nu \,\mathrm{Im}\, f_+(\nu)\, d\nu$ is *not* needed for our new constraints. Thus, the value of non-physical integrals, even if very large, does not affect our new constraints.

Having restricted ourselves so far to even amplitudes, let us now consider odd amplitudes. It is straightforward to show for odd amplitudes that FESR(odd) implies that

$$\frac{d^n\sigma_{\rm odd}}{d\nu^n}(\nu) = \frac{d^n\tilde{\sigma}_-}{d\nu^n}(\nu),\ n = 0, 1, 2, \ldots,\ \nu \geq \nu_0, \quad (18)$$

where $\tilde{\sigma}_-(\nu)$ is the odd (under crossing) high energy cross section approximation and $\sigma_{\rm odd}(\nu)$ is the experimental odd cross section.

Thus, we have now derived new analyticity constraints for *both even and odd cross sections*, allowing us to constrain both hh and $\bar{\rm h}$h scattering. Block and Halzen [2] expanded upon these ideas, using linear combinations of cross sections and derivatives to anchor *both* even and odd cross sections. A total of 4 constraints, 2 even and 2 odd constraints, were used by them in their successful $\ln^2 s$ fit to pp and $\bar{p}p$ cross sections and ρ-values, where they first did a local fit to pp and $\bar{p}p$ cross sections and their slopes in the neighborhood of $\nu_0 = 7.59$ GeV (corresponding to $\sqrt{s}_0 = 4$ GeV), to determine the experimental cross sections and their first derivatives at which they anchored their fit. The data they used in the high energy fit were pp and $\bar{p}p$ cross sections and ρ-values with energies $\sqrt{s} \geq 6$ GeV. Introducing the even cross section $\sigma_0(\nu)$, they parameterized the high energy cross sections and ρ values [2] as

$$\sigma_0(\nu) = c_0 + c_1 \ln\left(\frac{\nu}{m}\right) + c_2 \ln^2\left(\frac{\nu}{m}\right) + \beta_{\mathcal{P}'}\left(\frac{\nu}{m}\right)^{\mu-1}, \quad (19)$$

$$\sigma^{\pm}(\nu) = \sigma_0\left(\frac{\nu}{m}\right) \pm\ \delta\left(\frac{\nu}{m}\right)^{\alpha-1}, \quad (20)$$

$$\rho^{\pm}(\nu) = \frac{1}{\sigma^{\pm}}\left\{\frac{\pi}{2}c_1 + c_2\pi \ln\left(\frac{\nu}{m}\right) - \beta_{\mathcal{P}'}\cot\left(\frac{\pi\mu}{2}\right)\left(\frac{\nu}{m}\right)^{\mu-1} + \frac{4\pi}{\nu}f_+(0) \pm\ \delta\tan\left(\frac{\pi\alpha}{2}\right)\left(\frac{\nu}{m}\right)^{\alpha-1}\right\}. \quad (21)$$

We note that the even coefficients c_0, c_1, c_2 and $\beta_{\mathcal{P}'}$ are the same as those used in Eq. (16). The real constant $f_+(0)$ is the subtraction constant [7, 9] required at $\nu = 0$ for a singly-subtracted dispersion relation. They also used $\mu = 0.5$. The odd cross section in Eq. (20) is given by $\delta\left(\frac{\nu}{m}\right)^{\alpha-1}$, described by two parameters, the coefficient δ and the Regge power $\alpha < 1$, so that the difference cross section between pp and $\bar{p}p$ vanishes at high energies.

We now have new analyticity constraints for both even and odd amplitudes. The fits are anchored by the experimental cross section data near the transition energy ν_0. These consistency constraints are due to the application of analyticity to finite energy integrals—the analog of analyticity giving rise to traditional dispersion relations when it is applied to integrals with infinite upper limits.

γp, $\pi^{\pm}p$, $\bar{p}p$ and pp scattering. Using the 4 constraints of the previous Section, we show in Fig. 1 both the $\ln^2 s$ fit and the $\ln s$ fit of Eq. (19) and Eq. (20) to the experimental $\pi^{\pm}p$ total cross sections. The high energy fit is anchored to the very accurate data a at $\sqrt{s} = 2.6$ GeV. Because of the 4 constraints, the $\ln^2 s$ fit needs only to fit the two parameters c_1 and c_2, whereas the $\ln s$ fit sets $c_2 = 0$ and fits only c_1. We see that the $\ln^2 s$ fit, which *saturates the Froissart bound*, gives an excellent fit to the data, while the $\ln s$ fit is ruled out. Shown in Fig. 2 are the ρ-values for $\pi^{\pm}p$ scattering: again, we see that the $\ln s$ fit is ruled out, whereas we get a good fit when we saturate the Froissart bound.

In Fig. 3 we compare the results of our fitted πp cross section σ_0 (from Eq. (19)) with a rescaled version of $\sigma_0(\gamma p)$ that was obtained from a fit to all known high energy γp cross sections. From about $2 \leq \sqrt{s} \leq 300$ GeV, the two saturated $\ln^2 s$ fits are virtually indistinguishable. Thus we conclude that high energy γp total cross sections also go as $\ln^2 s$.

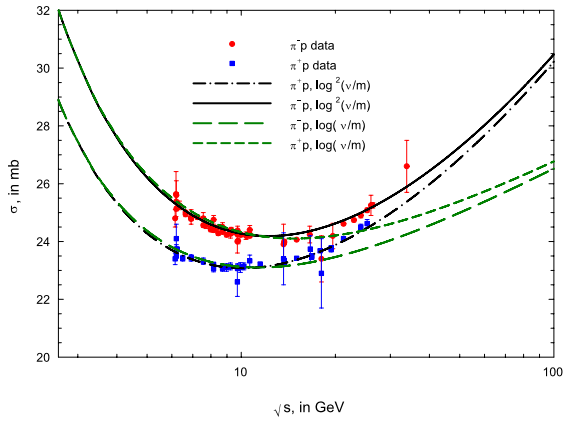

FIG. 1: The fitted total cross sections σ_{π^+p} and σ_{π^-p} in mb, *vs.* $\sqrt{s}$, in GeV, using 4 constraints. The circles are the sieved data for π^-p scattering and the squares are the sieved data for π^+p scattering for $\sqrt{s} \geq 6$ GeV. The dash-dotted curve (π^+p) and the solid curve (π^-p) are $\ln^2 s$ fits. The short dashed curve (π^+p) and the long dashed curve (π^-p) are $\ln s$ fits and clearly do *not* fit the data.

We next consider high energy $\bar{p}p$ and pp scattering. Shown in Fig. 4 are fits to the total cross sections, where again, for the $\ln^2 s$ fit, *only 2* parameters, c_1 and c_2 are

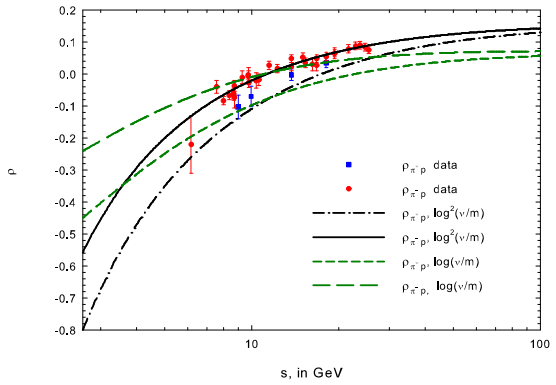

FIG. 2: The fitted ρ-values, $\rho_{\pi^+ p}$ and $\rho_{\pi^- p}$, *vs.* $\sqrt{s}$, in GeV, using 4 constraints. The circles are the sieved data for $\pi^- p$ scattering and the squares are the sieved data for $\pi^+ p$ scattering for $\sqrt{s} \geq 6$ GeV. The dash-dotted curve ($\pi^+ p$) and the solid curve ($\pi^- p$) are $\ln^2 s$ fits. The short dashed curve ($\pi^+ p$) and the long dashed curve ($\pi^- p$) are $\ln s$ fits, which again are bad fits to the experimental data.

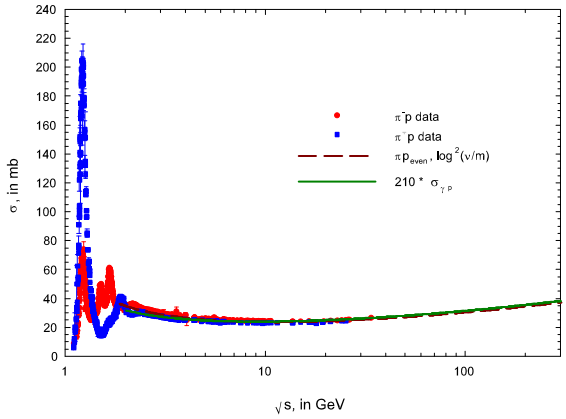

FIG. 3: The circles are the cross section data for $\pi^- p$ scattering and the squares are the cross section data for $\pi^+ p$ scattering, in mb, *vs.* $\sqrt{s}$, in GeV, for all of the known data. The dashed curve is the $\ln^2 s$ πp fit to the high energy cross section data of the even amplitude cross section, σ_0. The solid curve is the fit of the γp cross section data , for cms energies $\sqrt{s} \geq 2.01$ GeV, whereas the πp data (cross sections and ρ-values) were fit for cms energies $\sqrt{s} \geq 6$ GeV. The two fitted curves are virtually indistinguishable in the energy region $2 \leq \sqrt{s} \leq 300$ GeV.

fit, after anchoring the high energy data to the accurate cyclotron data at $\sqrt{s} = 4$ GeV. Once again, we see that we have an excellent $\ln^2 s$ fit to all of the high energy total cross section data when we anchor our fit (of only 2 parameters!) to the low energy data, whereas the $\ln s$ fit to these data fails. In Fig. 5 we compare the nucleon-nucleon ρ-values to our 3 parameter fit of c_0, c_1 and the subtraction constant $f_+(0)$.

Before employing the "Sieve" algorithm on the totality of 212 high energy $\bar{p}p$ and pp cross sections, the $\chi^2/d.f.$ was 5.7 for the $\ln^2 s$ fit, clearly an unacceptably high

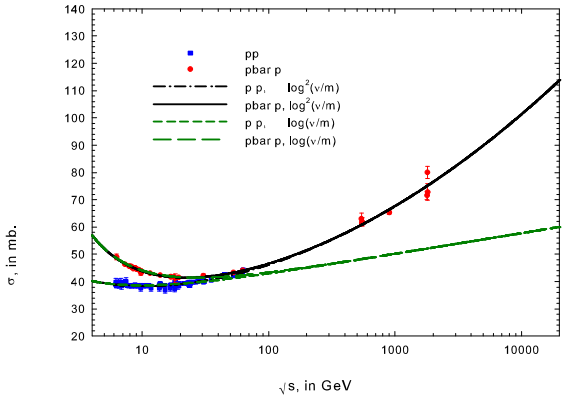

FIG. 4: The fitted total cross sections σ_{pp} and $\sigma_{\bar{p}p}$ in mb, *vs.* $\sqrt{s}$, in GeV, using 4 constraints. The circles are the sieved data for $\bar{p}p$ scattering and the squares are the sieved data for pp scattering for $\sqrt{s} \geq 6$ GeV. The dash-dotted curve (pp) and the solid curve ($\bar{p}p$) are $\ln^s$ fits to the high energy data. The short dashed curve (pp) and the long dashed curve ($\bar{p}p$) are $\ln s$ fits to the high energy data. Clearly, the $\ln s$ fits do *not* fit the experimental data.

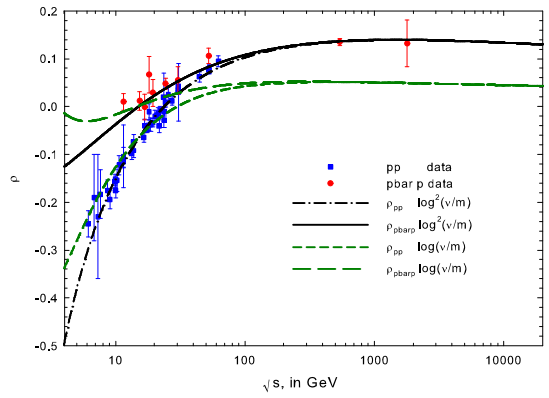

FIG. 5: The fitted ρ-values, ρ_{pp} and $\rho_{\bar{p}p}$, *vs.* $\sqrt{s}$, in GeV, using 4 constraints. The circles are the sieved data for $\bar{p}p$ scattering and the squares are the sieved data for pp scattering for $\sqrt{s} \geq 6$ GeV. The dash-dotted curve (pp) and the solid curve ($\bar{p}p$) are $\ln^2 s$ fits The short dashed curve (pp) and the long dashed curve ($\bar{p}p$) are $\ln s$ fits. Clearly, the $\ln s$ fits do *not* fit the experimental data.

value. After "sieving", the renormalized $\chi^2/d.f.$ was 1.09, for 184 degrees of freedom, using a $\Delta\chi_i^2 > 6$ cut. The total χ^2 was 201.4, corresponding to a probability of fit ≈ 0.2. In all, the 25 rejected points contributed 981 to the total χ^2, i.e., an *average* $\Delta\chi^2$ of about 39 per point!

For the LHC , the $\ln^2 s$ fits shown in Fig. 4 and Fig. 5 predict

$$\sigma_{pp} = 107.3 \pm 1.2 \text{ mb}, \ \sqrt{s} = 14 \text{ TeV} \quad (22)$$

$$\rho_{pp} = 0.132 \pm 0.001, \quad (23)$$

where the quoted errors are due to the uncertainties in the fit parameters.

Deep inelastic scattering (DIS). Berger, Block and Tan [3] analyzed the x dependence of the DIS proton structure

functions $F_2^p(x,Q^2)$ by beginning with the assumption that the x dependence at extremely small x should manifest a behavior consistent with saturation of the Froissart bound on hadronic total cross sections [1], as is satisfied by data on γp, $\pi^{\pm} p$, and $\bar{p}p$ and pp interactions. They treated DIS ep scattering as the hadronic reaction $\gamma^* p$, demanding that the total cross section $\sigma(\gamma^* p)$ saturate the Froissart bound of $\ln^2 s$. For the process $\gamma^* + p \to X$, the invariant s is given by $s = Q^2/x$, for small x, when $s \gg m^2$, where m is the proton mass, x is the fractional longitudinal momentum of the proton carried by its parton constituents and Q^2 is the virtuality of the γ^*. Thus, saturting the Froissart bound [1] demands that $F_2^p(x,Q^2)$ grow no more rapidly than $\ln^2(1/x)$ at very small x. Over the ranges of x and Q^2 for which DIS data are available, they show that a very good fit to the x dependence of ZEUS data [10] is obtained for $x \leq x_P = 0.09$ and $\frac{Q^2}{x} \gg m^2$ using the expression

$$F_2^p(x,Q^2) = (1-x) \times \Big\{ \frac{F_P}{1-x_P} + A(Q^2) \ln \left[\frac{x_P}{x} \frac{1-x}{1-x_P} \right] + B(Q^2) \ln^2 \left[\frac{x_P}{x} \frac{1-x}{1-x_P} \right] \Big\}. \quad (24)$$

Their fits to DIS data [10] at 24 values of Q^2 cover the wide range $0.11 \leq Q^2 \leq 1200$ GeV^2. The value $x_P = 0.09$ is a scaling point such that the curves for all Q^2 pass through the point $x = x_P$, at which $F_2(x_P, Q^2) = F_P \sim 0.41$, further constraining all of the fits. Figure 6 shows that also in $\gamma^* p$ scattering, the Froissart bound appears to be saturated.

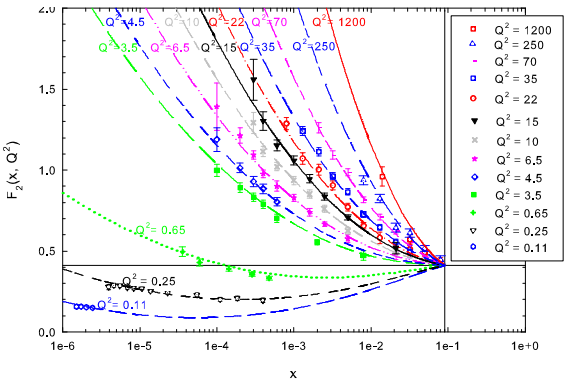

FIG. 6: Fits to the proton structure function data, $F_2^p(x,Q^2)$ vs. x of the form $\ln^2 s$, for 13 values of Q^2. The data are from the ZEUS collaboration [10]. The curves show 13 of 28 global fits [3]. The vertical and horizontal straight lines intersect at the scaling point $x_P = 0.09, F_2^p(x_P) = 0.41$.

The "Aspen" model. The "Aspen" model is a QCD-inspired eikonal model [11] which naturally yields total pp and $\bar{p}p$ cross sections that go as $\ln^2 s$ at large energies, i.e., they automatically saturate the Froissart bound. From

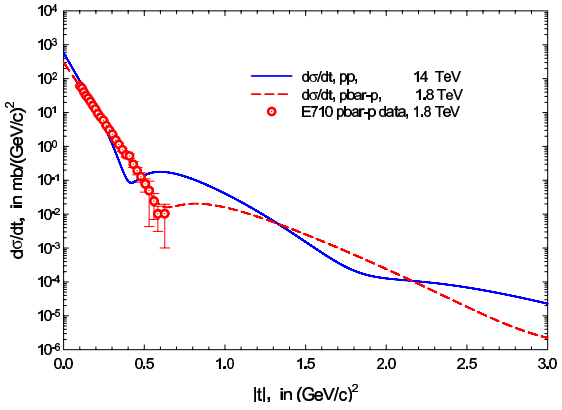

FIG. 7: The elastic differential scattering cross section $\frac{d\sigma}{dt}$, in mb/(GeV/c)^2 vs. $|t|$, in (GeV/c)^2, using a constrained Aspen Model fit (QCD-inspired theory). The solid curve is the prediction for the reaction $pp \to pp$ at the LHC, at $\sqrt{s} = 14$ TeV. The dashed curve is the prediction for the reaction $\bar{p}p \to \bar{p}p$ at $\sqrt{s} = 1.8$ TeV, at the Tevatron Collider; the data points are from the E710 experiment.

the model, one can extract the total cross section $\sigma_{\rm tot}$, the ρ-value, the elastic cross section $\sigma_{\rm el}$, the nuclear slope parameter B (the logarithmic derivative of $d\sigma_{\rm el}/dt$ at $t = 0$) and $d\sigma_{\rm el}/dt$ as a function of t, the squared 4-momentum transfer. Shown in Fig. 7 is a constrained Aspen-model fit [12] to $d\sigma_{\rm el}/dt$ vs. $|t|$, for 1.8 TeV , compared to E710 data at 1.8 TeV; the fit is excellent. Also shown is the prediction for the LHC, at 14 TeV. For more details af the model and for results for constrained total cross sections, etc., see Ref. [12].

Cosmic ray predictions. There are now available published [13–16] and preliminary [17, 18] p-air inelastic production cross sections ($\sigma^{\rm inel}_{p-{\rm air}}$) that span the enormous pp cms (center-of-mass system) energy range $0.1 \lesssim \sqrt{s} \lesssim 100$ TeV, reaching energies well above the Large Hadron Collider (LHC). Further, we expect high statistics results from the Pierre Auger Collaboration [19] in the near future in this ultra-high energy region. Most importantly, we now have available very accurate predictions at cosmic ray energies for the total pp cross section, σ_{pp}, from fits [20] to accelerator data that used adaptive data sifting algorithms [21] and analyticity constraints [22] that were not available in the earlier work of Block, Halzen and Stanev [23]. Here we take advantage of these new pp cross section predictions in order to make *accurate* predictions of the cosmic ray p-air total cross sections, to be compared with past and future experiments.

Extracting proton–proton cross sections from published cosmic ray observations of extensive air showers, and vice versa, is far from straightforward [24]. By a variety of experimental techniques, cosmic ray experiments map the atmospheric depth at which extensive air showers develop and measure the distribution of $X_{\rm max}$, the shower maximum, which is sensitive to the inelas-

tic p-air cross section $\sigma^{\rm inel}_{p-{\rm air}}$. From the measured $X_{\rm max}$ distribution, the experimenters deduce $\sigma^{\rm inel}_{p-{\rm air}}$. We will compare published [13–15] and recently announced preliminary values of $\sigma^{\rm inel}_{p-{\rm air}}$ with predictions made from σ_{pp}, using a Glauber model to obtain $\sigma^{\rm inel}_{p-{\rm air}}$ from σ_{pp}.

$\sigma^{\rm inel}_{p-{\rm air}}$ *from the* $X_{\rm max}$ *distribution: Method I.* The measured shower attenuation length (Λ_m) is not only sensitive to the interaction length of the protons in the atmosphere ($\lambda_{p-{\rm air}}$) [25], with

$$\Lambda_m = k\lambda_{p-{\rm air}} = k\frac{14.4m_p}{\sigma^{\rm inel}_{p-{\rm air}}} = k\frac{24,100}{\sigma^{\rm inel}_{p-{\rm air}}}\,, \qquad (25)$$

(with Λ_m and $\lambda_{p-{\rm air}}$ in g cm^{-2}, the proton mass m in g, and the inelastic production cross section $\sigma^{\rm inel}_{p-{\rm air}}$ in mb), but also depends on the rate at which the energy of the primary proton is dissipated into electromagnetic shower energy observed in the experiment. The latter effect is parameterized in Eq. (25) by the parameter k. The value of k depends critically on the inclusive particle production cross section and its energy dependence in nucleon and meson interactions on the light nuclear target of the atmosphere (see Ref. [24]). We emphasize that the goal of the cosmic ray experiments is $\sigma^{\rm inel}_{p-{\rm air}}$ (or correspondingly, $\lambda_{p-{\rm air}}$), whereas in Method I, the *measured* quantity is Λ_m. Thus, a significant drawback of Method I is that one needs a model of proton-air interactions to complete the loop between the measured attenuation length Λ_m and the cross section $\sigma^{\rm inel}_{p-{\rm air}}$, *i.e.,* one needs the value of k in Eq. (25) to compute $\sigma^{\rm inel}_{p-{\rm air}}$. Shown in Table I are the widely varying values of k used in the different experiments. Clearly the large range of k-values, from 1.15 for EASTOP [17] to 1.6 for Fly's Eye [13] differ significantly, thus making the *published* values of $\sigma^{\rm inel}_{p-{\rm air}}$ unreliable. It is interesting to note the monotonic decrease over time in the k's used in the different experiments, from 1.6 used in Fly's Eye in 1984 to the 1.15 value used in EASTOP in 2007, showing the time evolution of Monte Carlo models of energy dissipation in showers. For comparison, Monte Carlo simulations made by Pryke [26] in 2001 of several more modern shower models are also shown in Table I. Even among modern shower models, the spread is still significant: one of our goals is to minimize the impact of model dependence on the $\sigma^{\rm inel}_{p-{\rm air}}$ determination.

$\sigma^{\rm inel}_{p-{\rm air}}$ *from the* $X_{\rm max}$ *distribution: Method II.* The HiRes group [16] has developed a quasi model-free method of measuring $\sigma^{\rm inel}_{p-{\rm air}}$ directly. They fold into their shower development program a randomly generated exponential distribution of shower first interaction points, and then fit the entire distribution, and not just the trailing edge, as done in other experiments [13–15, 17]. They obtain $\sigma^{\rm inel}_{p-{\rm air}} = 460 \pm 14\,({\rm stat}) + 39\,({\rm syst}) - 11\,({\rm syst})$ mb at $\sqrt{s} = 77$ TeV, which they claim is effectively model-independent and hence is an absolute determination [16].

Extraction of σ_{pp} *from* $\sigma^{\rm inel}_{p-{\rm air}}$. The total pp cross section is extracted from $\sigma^{\rm inel}_{p-{\rm air}}$ in two distinct steps. First,

TABLE I: A table of k-values, used in experiments and from Monte Carlo model simulation

Experiment	k
Fly's Eye	1.6
AGASA	1.5
Yakutsk	1.4
EASTOP	1.15
Monte Carlo Results: C.L. Pryke	
Model	k
CORSIKA-SIBYLL	1.15 ± 0.05
MOCCA–SIBYLL	1.16 ± 0.03
CORSIKA-QGSjet	1.30 ± 0.04
MOCCA–Internal	1.32 ± 0.03

one calculates the p-air *total* cross section, $\sigma_{p-{\rm air}}$, from the measured inelastic production cross section using

$$\sigma^{\rm inel}_{p-{\rm air}} = \sigma_{p-{\rm air}} - \sigma^{\rm el}_{p-{\rm air}} - \sigma^{q-{\rm el}}_{p-{\rm air}}\,. \qquad (26)$$

Next, the Glauber method [27] is used to transform the measured value of $\sigma^{\rm inel}_{p-{\rm air}}$ into the pp total cross section σ_{pp}; all the necessary steps are calculable in the theory. In Eq. (26) the measured cross section for particle production is supplemented with $\sigma^{\rm el}_{p-{\rm air}}$ and $\sigma^{q-{\rm el}}_{p-{\rm air}}$, the elastic and quasi-elastic cross section, respectively, as calculated by the Glauber theory, to obtain the total cross section $\sigma_{p-{\rm air}}$. The subsequent relation between $\sigma^{\rm inel}_{p-{\rm air}}$ and σ_{pp} critically involves the nuclear slope parameter B, the logarithmic slope of forward elastic pp scattering, $d\sigma^{\rm el}_{pp}/dt$. A plot of B against σ_{pp}, 5 curves of different values of $\sigma^{\rm inel}_{p-{\rm air}}$, is shown in Fig. 8, taking into account inelastic screening [28]. The reduction procedure from $\sigma^{\rm inel}_{p-{\rm air}}$ to σ_{pp} is summarized in Ref. [24]. The solid curve in Fig. 8 is a plot of B vs. σ_{pp}—with B taken from the "Aspen" eikonal model and σ_{pp} taken from the $\ln^2 s$ fit using analytic amplitudes. The large dot corresponds to the value of σ_{pp} and B at $\sqrt{s} = 77$ TeV, the HiRes energy, thus fixing the HiRes predicted value of $\sigma^{\rm inel}_{p-{\rm air}}$.

Obtaining σ_{pp} *from* $\sigma^{\rm inel}_{p-{\rm air}}$. In Fig. 9, we have plotted the values of σ_{pp} vs. $\sigma^{\rm inel}_{p-{\rm air}}$ that are deduced from the intersections of the B-σ_{pp} curve with the $\sigma^{\rm inel}_{p-{\rm air}}$ curves in Fig. 8. Figure 9 furnishes cosmic ray experimenters with an easy method to convert their measured $\sigma^{\rm inel}_{p-{\rm air}}$ to σ_{pp}, and vice versa.

Determining the k value. In Method I, the extraction of $\lambda_{p-{\rm air}}$ (or $\sigma^{\rm inel}_{p-{\rm air}}$) from the measurement of Λ_m requires knowing the parameter k. The measured depth $X_{\rm max}$ at which a shower reaches maximum development in the atmosphere, which is the basis of the cross section measurement in Ref. [13], is a combined measure of the depth of the first interaction, which is determined by the inelastic cross section, and of the subsequent shower development, which has to be corrected for. The model dependent rate of shower development and its fluctuations are the origin of the deviation of k from unity in

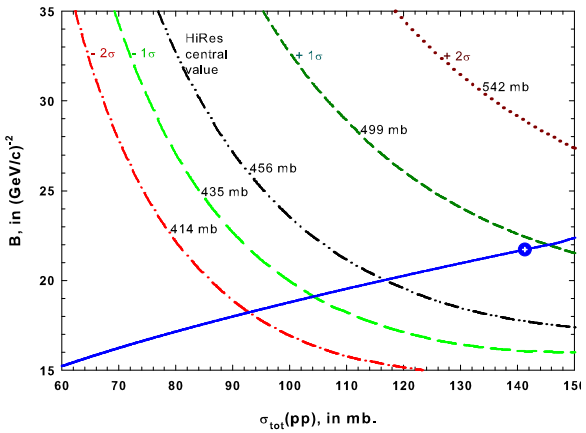

FIG. 8: B dependence on the pp total cross section σ_{pp}. The five curves are lines of constant $\sigma^{\rm inel}_{p-{\rm air}}$, of 414, 435, 456, 499 and 542 mb—the central value is the published Fly's Eye value, and the others are $\pm 1\sigma$ and $\pm 2\sigma$. The solid curve is a plot of a QCD-inspired fit of B against σ_{pp}, obtained from a $\ln^2 s$ fit. The large dot is the prediction for $\sigma^{\rm inel}_{p-{\rm air}}$ at $\sqrt{s} = 77$ TeV, the HiRes energy.

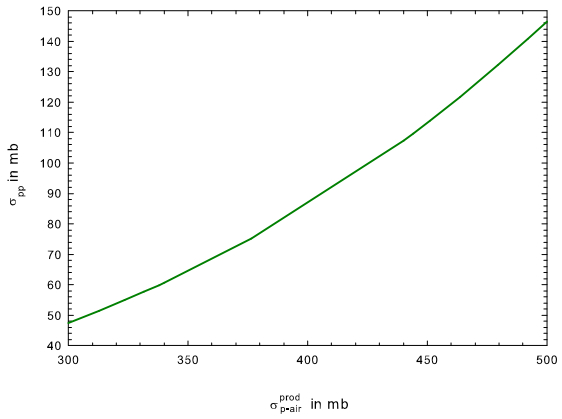

FIG. 9: A plot of the predicted total pp cross section σ_{pp}, in mb *vs.* the predicted production p-air cross section, $\sigma^{\rm inel}_{p-{\rm air}}$, in mb, where

Eq. (25). As seen in Table I, its values range from 1.6 for a very old model where the inclusive cross section exhibited Feynman scaling, to 1.15 for modern models with large scaling violations.

Adopting the same strategy that earlier had been used by Block, Halzen and Stanev [23], we matched the data to our prediction of $\sigma^{\rm inel}_{p-{\rm air}}(s)$, extracting a *common* value for k, neglecting the possibility of a weak energy dependence of k over the range measured, found to be very small in the simulations of Ref. [26]. By combining the results of B from the "Aspen" model and Fig. 9, we obtain our prediction of $\sigma^{\rm inel}_{p-{\rm air}}$ vs. $\sqrt{s}$, which is shown in Fig. 10. Leaving k as a free parameter,we make a χ^2 fit to *rescaled* $\sigma^{\rm inel}_{p-{\rm air}}(s)$ values of Fly's Eye, [13]AGASA [14], EASTOP [17] and Yakutsk [15], the experiments that need a common k-value.

Figure 10 is a plot of $\sigma^{\rm inel}_{p-{\rm air}}$ vs. $\sqrt{s}$, the cms energy in GeV, for the two different types of experimental extraction, using Methods I and II described earlier. Plotted *as published* is the HiRes value at $\sqrt{s} = 77$ TeV, since it is an absolute measurement. We have rescaled in Fig. 10 the published values of $\sigma^{\rm inel}_{p-{\rm air}}$ for Fly's Eye [13], AGASA [14], Yakutsk [15] and EAS-TOP [17], against our prediction of $\sigma^{\rm inel}_{p-{\rm air}}$, using the *common* value of $k = 1.264 \pm 0.033 \pm 0.013$ obtained from a χ^2 fit, and it is the rescaled values that are plotted in Fig. 10, along with the rescaled values of ARGO-YBJ [18], which were not used in the fit. The error in k of 0.033 is the statistical error of the χ^2 fit, whereas the error of 0.013 is the systematic error due to the error in the prediction of $\sigma^{\rm inel}_{p-{\rm air}}$. Clearly, we have an excellent fit, with complete agreement for all experimental points. Our analysis gave $\chi^2 = 3.19$ for 11 degrees of freedom (the low χ^2 is likely due to overestimates of experimental errors). We note that our k-value, $k = 1.264 \pm 0.033 \pm 0.013$, although somewhat too small for the very low energy ARGO-YBJ data, is about halfway between the values of CORSIKA-SIBYLL and CORSIKA-QSGSjet found in the Pryke simulations [26], as seen in Table I for model predictions. We next compare our measured k parameter with a recent direct measurement of k by the HiRes group [31]. They measured the exponential slope of the tail of their X_m distribution, Λ_m and compared it to the p-air interaction length $\lambda_{p-{\rm air}}$ that they found. Using Eq. (25), they deduced that a preliminary value, $k = 1.21 + 0.14 - 0.09$, in agreement with our value.

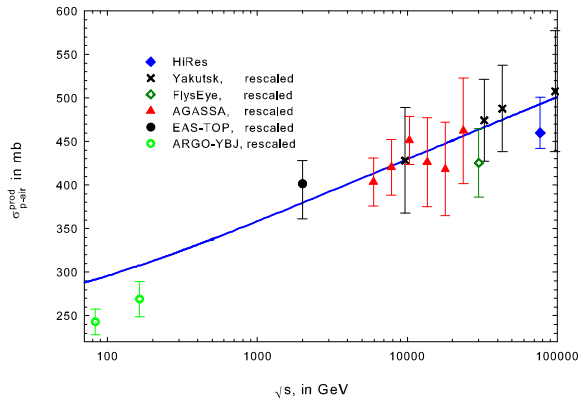

FIG. 10: A χ^2 fit of the *renormalized* AGASA, EASTOP, Fly's Eye and Yakutsk data for $\sigma^{\rm inel}_{p-{\rm air}}$, in mb, as a function of the energy, $\sqrt{s}$, in GeV. The result of the fit for the parameter k in Eq. (25) is $k = 1.263 \pm 0.033$. The HiRes point (solid diamond), at $\sqrt{s} = 77$ GeV, is model-independent and has *not* been renormalized. The renormalized ARGO-YBJ data were not used in the fit.

Taken together with the goodness-of-fit of our fitted k value and the fact that our value, $k = 1.264\pm0.033\pm0.013$ is compatible with the range of k values from theoretical models shown in Table I, the preliminary HiRes value [31] of $k = 1.21 + 0.14 - 0.09$ is additional experimental confirmation of our overall method for determining k, i.e., our assumptions that the k value is essentially energy-independent, as well as being independent of the very different experimental techniques for measuring air-showers. Our measured k value, $k = 1.264\pm0.033\pm0.013$, agrees very well with the preliminary k-value measured by the HiRes group, at the several parts per mil level; in turn, they both agree with Monte Carlo model simulations at the 5–10 part per mil level.

It should be noted that the preliminary EASTOP measurement [17]—at the cms energy $\sqrt{s} = 2$ TeV—is at an energy essentially identical to the top energy of the Tevatron collider, where there is an *experimental* determination of $\sigma_{\bar{p}p}$ [32], and consequently, no necessity for an *extrapolation* of collider cross sections. Since their value of $\sigma^{\rm inel}_{p-{\rm air}}$ is in excellent agreement with the predicted value of $\sigma^{\rm inel}_{p-{\rm air}}$, this anchors our fit at its low energy end. Correspondingly, at the high end of the cosmic ray spectrum, the absolute value of the HiRes experimental value of $\sigma^{\rm inel}_{p-{\rm air}}$ at 77 TeV—which requires *no knowledge* of the k parameter—is also in good agreement with our prediction, anchoring the fit at the high end. Thus, our $\sigma^{\rm inel}_{p-{\rm air}}$ predictions, which span the enormous energy range, $0.1 \lesssim \sqrt{s} \lesssim 100$ TeV, are consistent with cosmic ray data, for both magnitude and energy dependence.

Shown in Fig. 11 are *all* of the known pp and $\bar{p}p$ totl cross section data, including the cosmic ray points, spanning the energy region from 2 GeV to 80 TeV, fitted by the *same* $\ln^2 s$ (saturated Froissart bound) fit of the even cross section $\sigma_0 = (\sigma_{pp} + \sigma_{\bar{p}p})/2$.

CCCR: Cyclotrons to Colliders to Cosmic Rays. We have finally reached our goal. This long energy tale of accelerator experiments, extending over some 55 years, from those using cyclotrons to those using synchrotons and then, finally, to those using colliders, has now been unified with those experiments using high energy cosmic rays as their beams. The accelerator experiments had large fluxes and accurate energy measurements, allowing for precision measurements: the more precise, the lower the energy. On the other hand, the cosmic ray experiments always suffered from low fluxes of particles and poor energy determinations of their events, but made up for that by their incredibly high energies.

The ability to clean up accelerator cross section and ρ-value data by the Sieve algorithm, along with new fitting techniques using analyticity constraints in the form of anchoring high energy cross section fits to the value of low energy pp and $\bar{p}p$ experimental cross sections (and their energy derivatives) have furnished us with a precision fit—using the a $\ln^2 s$ form that saturates the Froissart Bound—which allows us to make accurate extrapolations into the LHC and cosmic ray regions, extrapolations guided by the principles of analyticity and unitarity embodied in the Froissart Bound.

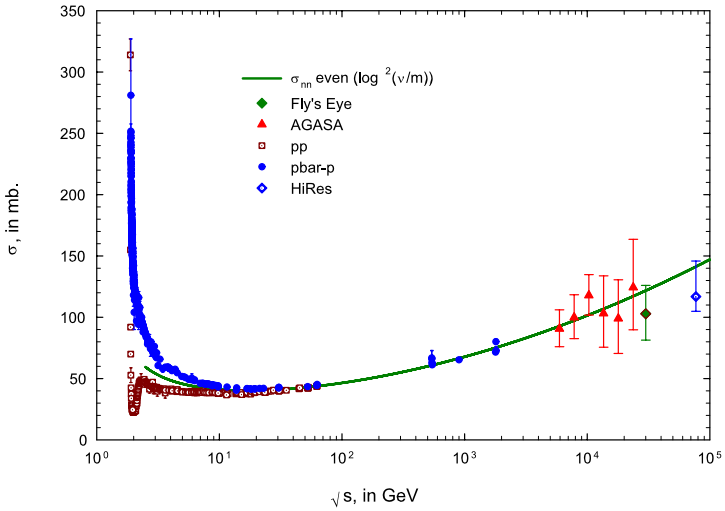

FIG. 11: All known [30] σ_{pp} and $\sigma_{\bar{p}p}$ accelerator total cross sections, shown together with σ_{pp} deduced from the AGASA, Fly's Eye and HiRes cosmic ray experiments. pp and $\bar{p}p$ accelerator total cross sections, in mb, vs. the c.m. energy $\sqrt{s}$, in GeV. The circles are $\bar{p}p$ and the open squares are pp data. The solid curve is a plot of σ_0, the even nucleon-nucleon cross section, taken from an analytically constrained global $\ln^2 s$ fit which included the cosmic ray data. The AGASA data are the triangles, the Fly's Eye point is the diamond and the HiRes point is the open diamond.

Acknowledgments. I wish to thank Peter Mazur , Larry Jones and the Aspen Center for Physics for making it possible for me to "give" this talk *in absentia*.

[1] M. Froissart, Phys. Rev. **123**, 1053 (1961).
[2] M. M. Block and F. Halzen, Phys. Rev D **70**, 091901 (2004); M. M. Block and F. Halzen, Phys. Rev D **72**, 036006 (2005).
[3] E. L. Berger, M. M. Block and C.-I Tan, Phys. Rev. Lett. **98**, 242001 (2007).
[4] M. M. Block, Eur. Phys. J. C **47**, 697 (2006).
[5] M. M. Block,Nucl. Instr. Meth. Phys. Res. A **556**, 308 (2006).
[6] K. Igi and M. Ishida, Phys. Rev D **66**, 034023 (2005); Phys. Lett. B **622**, 286 (2005).
[7] M. M. Block and R. N. Cahn, Rev. Mod. Phys. **57**, 563 (1985).
[8] R. Dolen, D. Horn and C. Schmid, Phys Rev. **166**, 178 (1968).
[9] M. Damashek and F. J. Gilman, Phys. Rev. D **1**, 1319 (1970)].
[10] ZEUS Collaboration, V. Chekanov et al, Eur. Phys. J. **21**, 443 (2001).
[11] M. M. Block, E. M. Gregores, F. Halzen, and G. Pancheri, Phys. Rev. D **58**, 017503 (1998).

[12] M. M. Block, Phys. Reports **36**, 71 (2006).

[13] R. M. Baltrusaitis *et al.*, Phys. Rev. Lett. **52**, 1380, 1984.

[14] M. Honda *et al.*, Phys. Rev. Lett. **70**, 525, 1993.

[15] S. P. Knurenko *et al.*, Proc 27th ICRC (Salt Lake City), Vol. 1, 372, 2001.

[16] K. Belov for the Hires Collaboration, Nucl Phys. B (Proc. Suppl,) **151**, 197, 2006.

[17] M. Aglietta *et al.*, Proc 25th ICRC (Durban) **6**, 37, 1997; G. Trinchero for the EASTOP Collaboration, 12th International Conference on Elastic and Diffractive Scattering - Forward Physics and QCD, Desy, Hamburg, May 21-25, 2007; G. Navarra for the EASTOP Collaboration, Aspen Workshop on Cosmic Ray Physics, April 15, 2007, http://cosmic-ray.physics.rutgers.edu/files; submitted to Phys. Lett. B.

[18] A. Surdo for the ARGO-YBJ Collaboration, Proceedings, European Cosmic Ray Symposium (2006);http://www.lip.pt/events/2006/ecrs/proc/ecrs06-s4-31.pdf.

[19] The Pierre Auger Project Design Report, Fermilab report (Feb. 1997); Paul Mantsch for the Pierre Auger Collaboration, arXiv:astro-ph/0604114v1, (2006).

[20] M. M. Block and F. Halzen, Phys. Rev. D **72**, 036006, 2005.

[21] M. M. Block, Nucl. Instrum. Methods A **556**, 308, 2006.

[22] M. M. Block, Eur. Phys J. C**47**, 697, 2006.

[23] M. M. Block, F. Halzen and T. Stanev, Phys. Rev. Lett. **83**, 4926, 1999; Phys. Rev. D **62** 77501, 2000.

[24] R. Engel *et al.*, Phys. Rev. D **58**, 014019, 1998.

[25] We will define "standard atmosphere" as the numerical relation given by Eq. (25), in order to have the density of nucleons needed to find the pp cross section from a nuclear model of "air". It would be useful for the experimenter to reduce his/her measurement to "standard atmosphere" so that it can be compared with other experiments, as well as with theory.

[26] C. L. Pryke, Astropart. Phys.14, 319, 2001.

[27] T. K. Gaisser *et al.*, Phys. Rev. D **36**, 1350, 1987.

[28] R. Engel, private communication, Karlsruhe, 2005.

[29] M. M. Block and F. Halzen, Phys. Rev. D **72**, 036006, 2005.

[30] Particle Data Group, K. Hagiwara S. Eidelman et al., Phys. Lett. **B592**, 1, 2004.

[31] K. Belov for the HiRes Collaboration, Aspen Workshop on Cosmic Ray Physics, April 15, 2007, http://cosmic-ray.physics.rutgers.edu/files/Belov-sigmapair.ppt .

[32] At $\sqrt{s} = 2$ TeV, the total cross sections $\sigma_{\bar{p}p}$ and σ_{pp} are expected to differ by ~ 0.01 mb, and thus, for the purpose of predicting $\sigma^{\rm inel}_{p-{\rm air}}$, are the same—see Ref. [**?**].